Adaptive optics in multiphoton microscopy: comparison of two, three and four photon fluorescence

David Sinefeld,[1,*] Hari P. Paudel,[2] Dimitre G. Ouzounov,[1] Thomas G. Bifano,[2] and Chris Xu[1]

[1]*School of Applied and Engineering Physics, Cornell University, Ithaca, NY, 14853, USA*
[2]*Boston University Photonics Center, Boston, MA, USA*
[*]*sinefeld@gmail.com*

Abstract: We demonstrate adaptive optics system based on nonlinear feedback from 3- and 4-photon fluorescence. The system is based on femtosecond pulses created by soliton self-frequency shift of a 1550-nm fiber-based femtosecond laser together with micro-electro-mechanical system (MEMS) phase spatial light modulator (SLM). We perturb the 1020-segment SLM using an orthogonal Walsh sequence basis set with a modified version of three-point phase shifting interferometry. We show the improvement after aberrations correction in 3-photon signal from fluorescent beads. In addition, we compare the improvement obtained in the same adaptive optical system for 2-, 3- and 4-photon fluorescence using dye pool. We show that signal improvement resulting from aberration correction grows exponentially as a function of the order of nonlinearity.

OCIS codes: (110.1080) Active or adaptive optics; (180.4315) Nonlinear microscopy; (180.2520) Fluorescence microscopy.

References and links

1. W. Denk, J. H. Strickler, and W. W. Webb, "Two-photon laser scanning fluorescence microscopy," Science **248**(4951), 73–76 (1990).
2. C. Xu, W. Zipfel, J. B. Shear, R. M. Williams, and W. W. Webb, "Multiphoton fluorescence excitation: new spectral windows for biological nonlinear microscopy," Proc. Natl. Acad. Sci. U.S.A. **93**(20), 10763–10768 (1996).
3. P. Theer, M. T. Hasan, and W. Denk, "Two-photon imaging to a depth of 1000 μm in living brains by use of a Ti:Al$_2$O$_3$ regenerative amplifier," Opt. Lett. **28**(12), 1022–1024 (2003).
4. D. Kobat, M. E. Durst, N. Nishimura, A. W. Wong, C. B. Schaffer, and C. Xu, "Deep tissue multiphoton microscopy using longer wavelength excitation," Opt. Express **17**(16), 13354–13364 (2009).
5. J. N. D. Kerr and W. Denk, "Imaging in vivo: watching the brain in action," Nat. Rev. Neurosci. **9**(3), 195–205 (2008).
6. D. A. Dombeck, C. D. Harvey, L. Tian, L. L. Looger, and D. W. Tank, "Functional imaging of hippocampal place cells at cellular resolution during virtual navigation," Nat. Neurosci. **13**(11), 1433–1440 (2010).
7. J. C. Jung, A. D. Mehta, E. Aksay, R. Stepnoski, and M. J. Schnitzer, "In vivo mammalian brain imaging using one- and two-photon fluorescence microendoscopy," J. Neurophysiol. **92**(5), 3121–3133 (2004).
8. D. Kobat, N. G. Horton, and C. Xu, "In vivo two-photon microscopy to 1.6-mm depth in mouse cortex," J. Biomed. Opt. **16**(10), 106014 (2011).
9. N. G. Horton, K. Wang, D. Kobat, C. G. Clark, F. W. Wise, C. B. Schaffer, and C. Xu, "In vivo three-photon microscopy of subcortical structures within an intact mouse brain," Nat. Photonics **7**(3), 205–209 (2013).
10. D. Ouzounov, N. Horton, T. Wang, D. Feng, N. Nishimura, and C. Xu, "In vivo three-photon calcium imaging of brain activity from layer 6 neurons in mouse brain," in *CLEO: 2014 Postdeadline Paper Digest*, OSA Technical Digest (online) (Optical Society of America, 2014), paper STh4C.2.
11. R. K. Tyson, *Principles of Adaptive Optics*, 3rd ed. (CRC, 2010).
12. Editorial, "Nature photonics technology focus: adaptive optics," Nat. Photonics **5**, 15–28 (2011).
13. M. J. Booth, "Adaptive optics in microscopy," Philos. Trans. A Math. Phys. Eng. Sci. **365**(1861), 2829–2843 (2007).
14. I. M. Vellekoop and A. P. Mosk, "Focusing coherent light through opaque strongly scattering media," Opt. Lett. **32**(16), 2309–2311 (2007).

15. I. M. Vellekoop, A. Lagendijk, and A. P. Mosk, "Exploiting disorder for perfect focusing," Nat. Photonics **4**(5), 320–322 (2010).
16. O. Katz, E. Small, and Y. Silberberg, "Looking around corners and through thin turbid layers in real time with scattered incoherent light," Nat. Photonics **6**(8), 549–553 (2012).
17. N. Ji, D. E. Milkie, and E. Betzig, "Adaptive optics via pupil segmentation for high-resolution imaging in biological tissues," Nat. Methods **7**(2), 141–147 (2010).
18. C. Wang, R. Liu, D. E. Milkie, W. Sun, Z. Tan, A. Kerlin, T.-W. Chen, D. S. Kim, and N. Ji, "Multiplexed aberration measurement for deep tissue imaging in vivo," Nat. Methods **11**(10), 1037–1040 (2014).
19. J. Tang, R. N. Germain, and M. Cui, "Superpenetration optical microscopy by iterative multiphoton adaptive compensation technique," Proc. Natl. Acad. Sci. U.S.A. **109**(22), 8434–8439 (2012).
20. L. Kong and M. Cui, "In vivo neuroimaging through the highly scattering tissue via iterative multi-photon adaptive compensation technique," Opt. Express **23**(5), 6145–6150 (2015).
21. O. Katz, E. Small, Y. Guan, and Y. Silberberg, "Noninvasive nonlinear focusing and imaging through strongly scattering turbid layers," Optica **1**(3), 170–174 (2014).
22. K. Wang, N. G. Horton, K. Charan, and C. Xu, "Advanced fiber soliton sources for nonlinear deep tissue imaging in biophotonics," IEEE J. Sel. Top. Quantum Electron. **20**, 6800311 (2014).
23. K. Wang and C. Xu, "Tunable high-energy soliton pulse generation from a large mode- area fiber and its application to third harmonic generation microscopy," Appl. Phys. Lett. **99**(7), 071112 (2011).
24. T. A. Pologruto, B. L. Sabatini, and K. Svoboda, "ScanImage: flexible software for operating laser scanning microscopes," Biomed. Eng. Online **2**(1), 13 (2003).
25. C. Stockbridge, Y. Lu, J. Moore, S. Hoffman, R. Paxman, K. Toussaint, and T. Bifano, "Focusing through dynamic scattering media," Opt. Express **20**(14), 15086–15092 (2012).
26. F. Wang, "Utility transforms of optical fields employing deformable mirror," Opt. Lett. **36**(22), 4383–4385 (2011).
27. H. P. Paudel, C. Stockbridge, J. Mertz, and T. Bifano, "Focusing polychromatic light through strongly scattering media," Opt. Express **21**(14), 17299–17308 (2013).
28. H. Schreiber and J. Bruning, *Optical Shop Testing* (John Wiley and Sons, Inc., 2006).
29. C. Xu and W. W. Webb, *Topics in Fluorescence Spectroscopy*, vol. 5 (Springer, 1997).
30. L. C. Cheng, N. G. Horton, K. Wang, S. J. Chen, and C. Xu, "Measurements of multiphoton action cross sections for multiphoton microscopy," Biomed. Opt. Express **5**(10), 3427–3433 (2014).
31. R. Noll, "Zernike polynomials and atmospheric turbulence," J. Opt. Soc. Am. **66**(3), 207–211 (1976).
32. M. Born and E. Wolf, *Principles of Optics*, 7th ed. (Cambridge University Press, 1999).
33. J. C. Wyant and K. Creath, "Basic wavefront aberration theory for optical metrology," in *Applied Optics and Optical Engineering*, J. C. Wyant, and R. R. Shannon, eds. (Academic Press, 1992), pp. 2−53.
34. D. Burke, B. Patton, F. Huang, J. Bewersdorf, and M. J. Booth, "Adaptive optics correction of specimen-induced aberrations in single-molecule switching microscopy," Optica **2**(2), 177–185 (2015).
35. M. J. Booth, D. Débarre, and A. Jesacher, "Adaptive optics for biomedical microscopy," Opt. Photonics News **23**(1), 22–29 (2012).

1. Introduction

Adaptive optics (AO) in multiphoton microscopy is a combination of two powerful modern optical techniques: multiphoton laser scanning microscopy, which is based on nonlinear fluorescence excitation, together with adaptive beam shaping using spatial light modulators (SLM). These two methods have been used during the past decades to allow imaging through inhomogeneous samples. Such samples, which are typical of biological tissues, induce aberrations and scattering to the light traveling through them, limiting the resolution and imaging depth of high resolution microscopy. During the past decade, both methods manage to demonstrate their ability to improve significantly both imaging depth and resolution.

Multiphoton fluorescence microscopy (MPM) is a well-established technique for deep-tissue imaging with subcellular resolution [1–4]. In fact, 2-photon laser scanning microscopy (2PM) is currently one of the main optical tools in *in vivo* mouse brain imaging, which allows the visualization of a single neuron and neuronal processes in a living brain [5–8]. In the last couple of years it was shown that higher order nonlinear microscopy, e.g. 3-photon fluorescence microscopy (3PM), when combined with long wavelength excitation, allows to achieve deeper imaging than 2PM. This method was found to be particularly useful for volumetric mouse brain imaging [9,10], because out-of-focus background generation can be further reduced due to the higher order nonlinear excitation.

AO techniques are very effective in correcting the aberrations induced by sample index mismatch and low order wavefront distortion in tissues [11–13]. In the last couple of years

AO techniques were applied also for scattering compensation even for cases where no unscattered 'ballistic' light component remains [14–16]. However, the small field-of-view of the corrected system [16] limits the ability to implement such correction in practical *in vivo* microscopy applications. The combination of MPM and AO was demonstrated for 2-photon adaptive optics fluorescence microscopy [17–20], resulting in improvement in signal and resolution compared to uncorrected systems. Signal improvement factors of 5-20 for imaging depth up to 400 μm were demonstrated [17–20]. Recently, it was theoretically shown that the compensation for signal degradation due to scattering will be much more significant in higher order nonlinear imaging techniques such as 3PM than in 2PM [21]. The same arguments are valid for low order aberration correction systems. Therefore, adaptive optics in 3PM will be potentially more important than for the 2-photon case, and have the opportunity to improve dramatically both imaging depth and resolution in biological tissues.

Here, we present what is to our best knowledge the first experimental demonstration of higher order nonlinear (3-photon and 4-photon) adaptive optics system. We use our system to show experimentally that higher order nonlinear feedback is much more effective than in the case of 2-photon excitation. In this paper, we focus on lower order aberration compensation (rather than scattering compensation) which is more effective for practical imaging with larger field of view. We demonstrate that for the same optical system and AO algorithm, signal improvement resulting from aberration correction grows exponentially as a function of the order of the nonlinear process. These results are important for AO in nonlinear microscopy, particularly for deep tissue imaging.

2. System description

A schematic description of the system is shown on Fig. 1(a). We use a compact, fiber-based femtosecond laser (Calmarlasers), delivering linearly polarized pulses with 500 fs pulse width and 1 MHz repetition rate at 1550 nm. The laser has up to 1.5W average power and is coupled into a 44-cm long photonic crystal (PC) rod (NKT Photonics) with an effective mode area of ~4400 μm^2. By increasing the input power, the output light can be shifted to a longer wavelength due to soliton self-frequency shift (SSFS) [22] inside the PC rod. In this way we can tune the center wavelength in the range between 1600 nm and 1700 nm [23].

For brain imaging purposes, it is preferable to use longer wavelengths (~1675-1700 nm) in order to exploit optimally the attenuation spectrum of the tissue [9]. However, in this experiment we want to use the same excitation wavelength to perform 2PM, 3PM and 4PM so that we can compare AO in exactly the same optical setup. We therefore adjust the input power to 800 mW (800 nJ per pulse at 1MHz) in order to shift the center wavelength to 1610 nm, resulting in pulse energy of 100 nJ per pulse after filtering out the residual pump with a 1580 nm long-pass filter (LPF). The pulse width of the soliton was measured by performing second-order autocorrelation (AC), and by assuming a *sech²(τ)* intensity profile, was found to be ~115 fs [Fig. 1(b)-top]. Due to the dispersion of the optical elements of the rest of the system (e.g., microscope optics), the pulse width broadened to 130 *fs* after the objective [Fig. 1(b)-bottom]. The output of the PC rod is collimated and projected onto a high speed, 1020-segment MEMS SLM (Boston Micromachines Corporation, Kilo-DM). The SLM was calibrated to support 2π phase stroke at 1610 nm using a fast high-voltage driver (Boston Micromachines Corporation S-Driver). The beam is then relayed onto a laser scanning system, where the SLM plane is imaged on both scan mirrors (Thorlabs) and then onto the back aperture of a 1.05 NA, water-immersion microscope objective (Olympus, XLPLN25XWMP). The objective aperture diameter is 15 mm and it is imaged on the SLM (10 × 10 mm^2 aperture) with × 0.5 magnification, resulting in 7.5 mm diameter on the SLM plane [Fig. 2(a)]. The objective aperture is slightly underfilled with a Gaussian beam diameter of 12 mm (1/e^2).
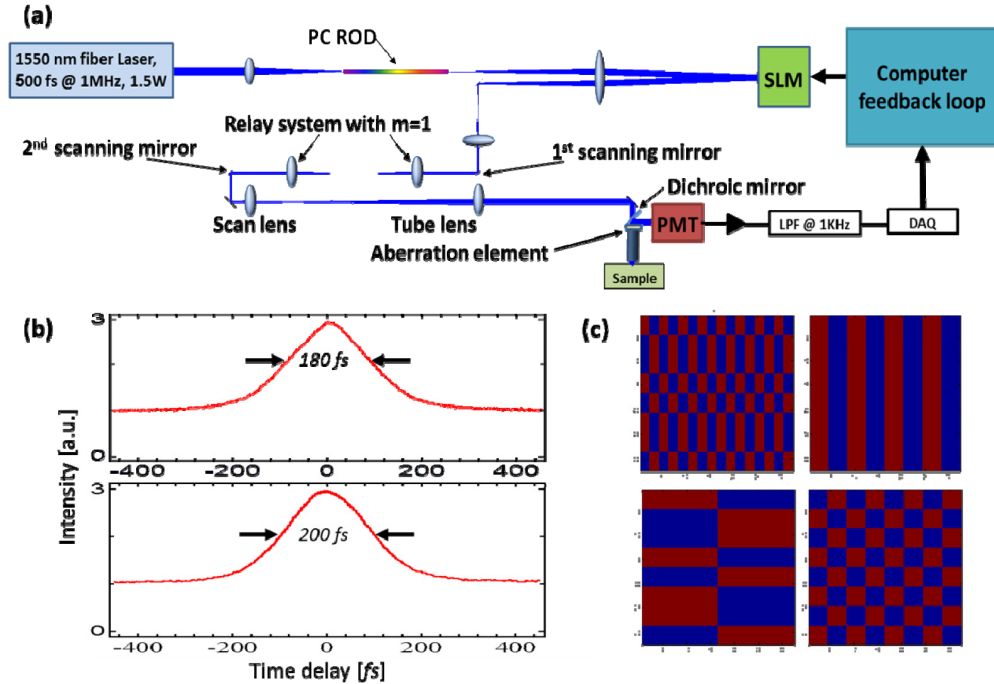
Fig. 1. (a) System description. The same excitation light is used for 2-, 3- and 4- photon fluorescence by changing the fluorescence dye, the PMT and the filter. (b) Second-order AC traces taken after the PC rod (top) and after the objective (bottom). The pulse FWHM values correspond to 115 fs (top) and 130 fs (bottom). (c) 4 Examples for Walsh binary phase patterns (out of 1024 patterns).

The generated fluorescence signal is reflected using a dichroic beamsplitter (Semrock FF875-Di01-25x36), and then split using a second dichroic beamsplitter (Semrock Di02-R561-25X36) onto two detectors: GaAs Photomultiplier tube (PMT, Hamamatsu H7422-50) and Ultra Bialkali (UBA) PMT (Hamamatsu R7600-200).The signal from the PMT is amplified for image generation using ScanImage [24]. A portion of the signal is used for feedback, and is sampled at 1.25 MHz (using NI PCI-6251 DAQ). With averaging of 2000 samples per measurement, we achieve a closed loop speed of ~300 Hz (including all system latencies caused by the computer control). The optical output power after the PC-rod was monitored using an optical sampler and a photodiode and controlled using a motorized half waveplate (HWP) and a polarization beamsplitter after the PC rod [not shown in Fig. 1].

3. Feedback algorithm and operation method

The feedback mechanism is based on parking the beam on a certain spot and optimizing the measured fluorescence signal. Since the generated fluorescence signal is a nonlinear function of the focal spot intensity, a smaller spot size will produce a significantly higher nonlinear signal, which can serve as a feedback [19–21]. We perturb the SLM using Walsh sequences which are semi-random orthogonal binary phase patterns [Fig. 1(c)] in order to find the compensation phase. Although originally developed for scattering compensation of monochromatic light [25,26], this approach is useful for both high order (scattering compensation) and low order aberration correction, as well as for polychromatic light [27]. Since the feedback loop speed is ~300 Hz, a full 1024 sequence can be completed within a few seconds. During the phase optimization process, $\pm \lambda/\alpha$ phase stroke is applied for each phase pattern, (usually, but not necessarily α is chosen to be 4 to apply ¼ of a wave) [25]. The collected signals (s_{i+} and s_{i-}) are used to calculate the multiplication constant C_i for pattern i

according to the three-point phase shifting interferometry (PSI) equation [25,28]. Since the phase response itself is nonlinear and corresponds to $cos^{2N}(\phi/2)$, as will be discussed in more detail in section 5, the equation for calculating C_i should be modified by taking the N_{th}-root of the input signals, where N is the order of the nonlinearity:

$$C_i = \tan^{-1}\left[\frac{\sqrt[N]{S_{i+}} - \sqrt[N]{S_{i-}}}{2\sqrt[N]{S_i} - \sqrt[N]{S_{i+}} - \sqrt[N]{S_{i-}}} \tan\left(\frac{\pi}{\alpha}\right) \right] \tag{1}$$

The examined pattern is added to the current phase applied on the SLM with the calculated weight C_i. Therefore, to complete the full sequence $3 \times 1024 = 3072$ iterations are needed. The sequences continue until there is no longer measurable improvement in the signal.

4. 3PM fluorescence beads experiment

In order to demonstrate the convergence of the algorithm experimentally, we used 200-nm red fluorescent beads (FluoSpheres, 580Ex/605Em) fixed in agarose gel. We first used a soliton pulse shift to 1660 nm and compensated for system aberration [Figs. 2(a-b)]. The initial axial resolution measured before correction was ~3.1 μm, where after correction an improved resolution of ~2.1 μm FWHM [Fig. 2(b), green line] was obtained. The theoretical limit for the axial resolution was estimated using the system parameters, resulting in an axial resolution of ~2 μm FWHM, in a close agreement to the experimental results.
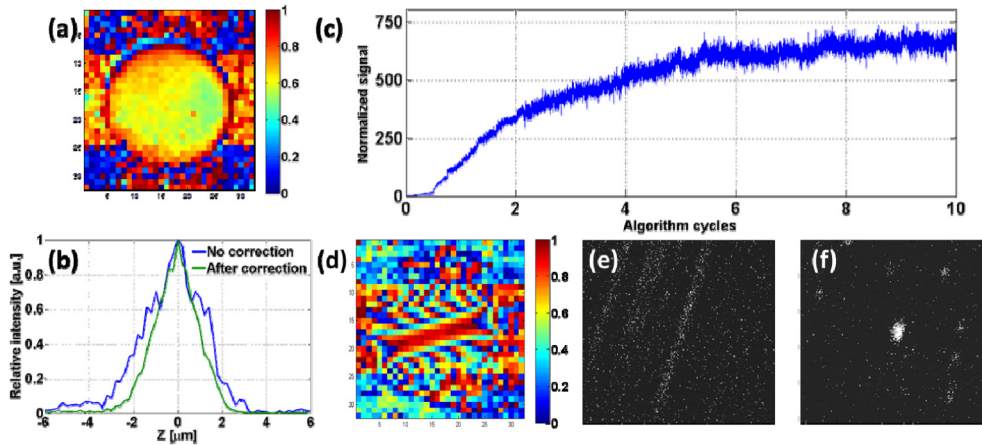

Fig. 2. Aberration correction results for 3-photon fluorescence from 200 nm fluorescent beads. (a-b) compensation for system aberrations: (a) System phase correction as it applied on the SLM, (b) Axial response before and after system correction. (c-f) Phase correction for 1-m focal length cylindrical lens: (c) Algorithm convergence with 200 nm beads as the test sample. (d) Phase correction applied on the SLM (color bar is in wavelength unit scale). (e-f): 3-photon images of beads: before (e) and after (f) phase correction. (Image size: 25 × 25 μm).

In order to show aberration compensation we used a cylindrical lens with $f = 1000$ mm placed above the objective aperture. Ten cycles of 1024 iterations were implemented, and the convergence process leads to approximately 700 times improvement in signal strength [Fig. 2(c)]. It is important to note that in order to avoid fluorescence saturation, the excitation power must be reduced during the optimization (this is done by controlling the HWP). The results shown in Fig. 2c are normalized to the N_{th} power of the input power (measured with the photodiode after the PC-rod), e.g. for 3PM the fluorescence signal is normalized to the cube of the input power.

The final phase of the SLM after correction is shown in Fig. 2(d). After the correction was completed, images were scanned with [Fig. 2(f)] and without [Fig. 2(e)] phase correction. The

images before and after AO correction reveal an uncertainty in calculating the exact improvement factor using fluorescent beads: since the starting point is ambiguous, different starting positions will yield different improvement factors. Indeed, repeating the same experiment with deliberate slight changes in the initial position of the bead (lateral or axial) resulted in different improvement factors but always with a centered bead after the correction. This is due to the fact that the algorithm adds phase in order to center the bead (tilting phase in case of lateral movement and power in case of axial movement), while changing the improvement factor. Although this is not a problem in general for an AO system which should just optimize the available signal to maximum, it is inconvenient for an experiment in which different samples are being measured using various orders of nonlinear excitation and the resulting improvement factors compared. In order to conduct such an experiment it is preferred to use a "dye pool" sample. In such a sample the exact position of the focal point in the sample does not change the signal, and making the comparison easier and more robust.

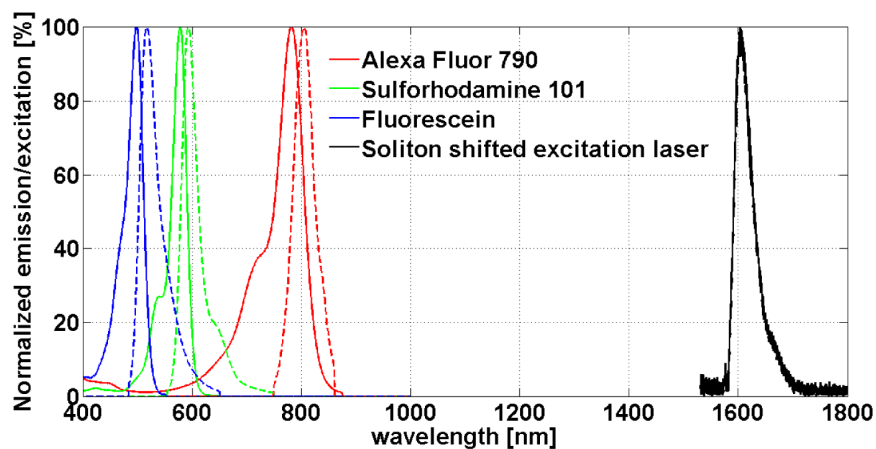## 5. Dye pool experiment – two, three and four photon fluorescence comparison

Fig. 3. The spectrum of the soliton-shifted excitation laser (black) and emission (dashed lines) and excitation (solid lines) spectra of Alexa Fluor 790, Sulforhodamine 101 and Fluorescein used for 2-, 3- and 4-photon fluorescence excitation, respectively. Data for the fluorescent dyes were obtained from Life Technologies, USA. http://www.lifetechnologies.com

To compare the AO performance for 2-, 3- and 4-photon fluorescence excitation, we used a 1610 nm soliton shift pulse with three different dyes [see Fig. 3]: 2-photon excitation with Alexa Fluor® 790 (785Ex/805Em), 3-photon excitation with Sulforhodamine 101 (SR101, 577Ex/593Em), and 4-photon excitation with Fluorescein (FITC, 499Ex/516Em). The 2- and 3-photon fluorescence were collected with the GaAs PMT using, respectively, a 790-nm LPF and a 630/92 nm bandpass filter (BPF). The 4-photon fluorescence was collected with the UBA PMT with a 535/50 nm BPF. The sample was prepared in a deep well microscope slide with a well depth of ~300 μm. The focal spot was set ~100 μm away from the water/glass interface to prevent significant third harmonic generation (THG) which may interfere with the measurements.

We measured the power-dependence curves [29,30] for each dye to verify the nonlinear orders [Fig. 4(a)]. To test the SLM performance for different nonlinear orders, we measure phase curves using the chess pattern shown in the lower right corner of Fig. 1(c). The results, shown in Fig. 4(b), shows a good match to $a + b \times \cos(\phi/2)^{2N}$, where N is the nonlinear order, ϕ is the phase difference between the different element of the chess pattern, and a and b are constants that depend on the applied pattern. This result verifies that it is reasonable to use Eq. (1) even for the dye pool experiment. After taking the N_{th} root of the signal it becomes the

same equation that was used for three-points PSI [25,28]. One should note that for different Walsh binary phase patterns, there are different values of *a* and *b*. This difference is more significant for 2-photon excitation, where for 3- and 4-photon excitation, the changes in *a* and *b* values for different patterns are much less pronounced.
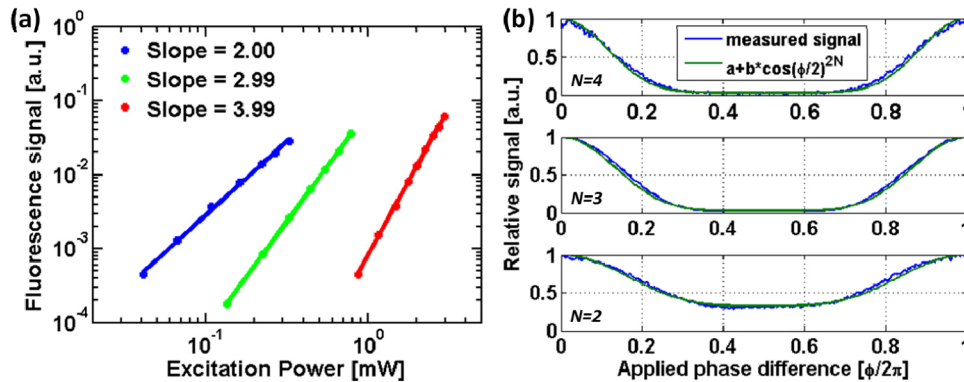

Fig. 4. (a) Power curves: Logarithmic plots of the dependence of 4-, 3-, and 2-photon excited fluorescence on excitation intensity for Alexa Fluor 790 (red square), Sulforhodamine 101 (green square) and Fluorescein (blue square). (b) Phase curves for N = 4, 3, and 2, obtained by applying alternating phase different with the chess pattern phase shown in the lower right part of Fig. 1. The results match the function: $a + b \times \cos(\phi/2)^{2N}$. The same signal levels were used for all experiments.

We used the algorithm described in section 3 to correct for system aberrations and for low-order aberrations of a cylindrical lens that was placed above the objective. We fixed the position of the cylindrical lens, and used a precision translation stage (Sutter Instrument Company) to load each sample to the same *z*-position. In this way, we made sure that we can replace the dyes without imposing any change onto the illumination system to ensure a fair comparison between different nonlinear orders. As shown in Fig. 4(a), we used the same signal levels, and therefore the same signal-to-noise ratios, for all dye experiments, and reduced input power during optimization in order to avoid saturation. We used cylindrical lenses with focal lengths of 2, 5 and 10m (the 5-m lens was a combination of two 10-m lenses). Convergence results and final phases for the 2-m cylindrical lens are shown in Fig. 5. For every experiment 20 iteration cycles were performed. It is easy to see that the improvement in signal becomes much larger for higher order nonlinear excitation. Since the sensitivity for aberration is higher for higher order nonlinearity, the convergence is also faster for higher order processes.

It should be noted that the results in Fig. 5 were taken with averaging over more samples per measurement compared to the beads (in which we used 2k samples per measurement). Furthermore, in order to have good convergence, we doubled the number of samples for the lower order nonlinearity, resulting in 20k, 40k and 80k samples per measurement for 4-, 3- and 2-photon excitation, respectively. Since the signal levels were similar for all the measurements, it means that the time required for convergence for 2-photon excitation is even longer than it appears in Fig. 5 since each cycle is twice as long as for 3-photon excitation and four times as long as for 4-photon excitation. Another interesting result is that the final phase map after convergence is different for 2-photon excitation when compared to those of the 3- and 4-photon excitation (the phase maps for 3- and 4-photon excitation are similar except for a constant phase that slightly changes the color map but does not affect the phase shape). The reason for this is again the fact that the sensitivity for aberration is lower for 2-photon excitation, which makes it harder for the algorithm to reach the right phase correction.

We used the phase map that was found in the 4-photon excitation experiment as a correction phase map for the 3- and 2-photon excitation experiments. While in the 3-photon

case there was no change in the improvement factor (compared to the phase map that the 3-photon signal based algorithm found), in the 2-photon case the improvement factor was slightly higher, resulting in × 2.35 instead of × 2.1 which was originally achieved using 2-photon signal.
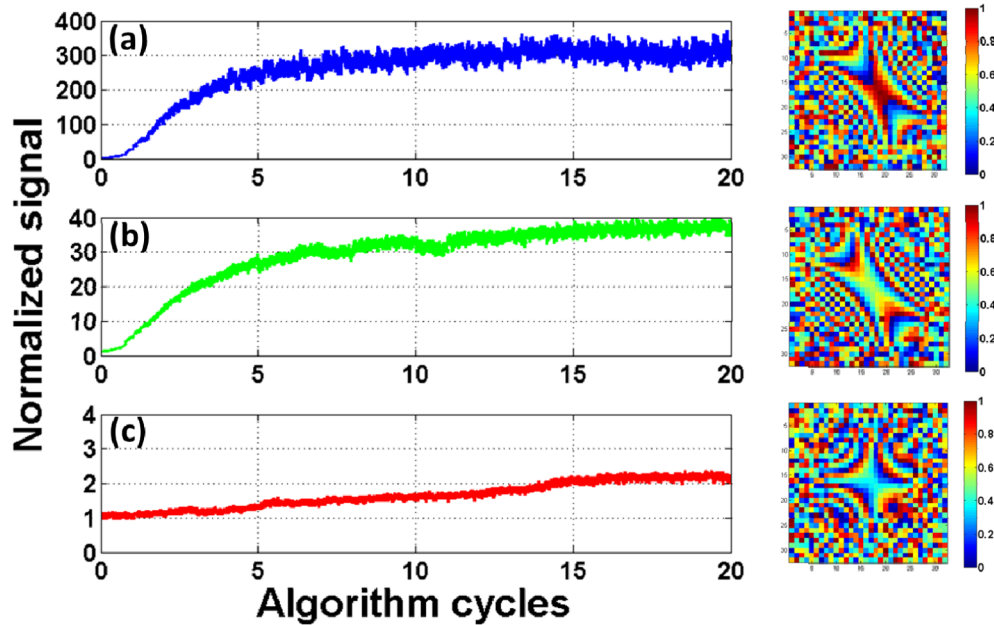

Fig. 5. Phase correction for a 2-m-focal length cylindrical lens for 2-, 3- and 4- photon excited fluorescence of Alexa Fluor 790, Sulforhodamine 101 and Fluorescein. (a) Left – 4-photon fluorescence convergence curve showing a signal improvement factor of × 320. Right – final phase applied on the SLM (b) left – 3-photon fluorescence convergence curve showing a signal improvement factor of × 40. Right – final phase applied on the SLM. (c) Left – 2-photon fluorescence convergence curve showing a signal improvement factor of × 2.1. Right – final phase applied on the SLM. Color-bars are in wavelength unit scale.

We repeated the experiment using the algorithm, compensating for system aberrations and for the 3 cylindrical lenses, for 2-, 3- and 4-photon excitation. The final phase correction maps for system aberration and the cylindrical lenses, taken from the 4-photon excitation optimization process, are shown in Fig. 6(a-d). In order to determine attenuation of the signal caused by the aberration, and in order to estimate the improvement factor for system and the cylindrical-lens correction, we measured power curves for each case (the example in Fig. 6(e) shows the case for 4-photon excitation with 2-m focal length cylindrical lens). The offset between the power curves is the improvement factor (or attenuation) in logarithmic scale. In addition, the power curve measurements ensured that the signal curves had the expected nonlinearity. We should note that for calculating signal degradation, we excluded the lens transmission attenuation, by dividing the attenuation results with the N_{th} power of the transmission coefficients which were measured separately.
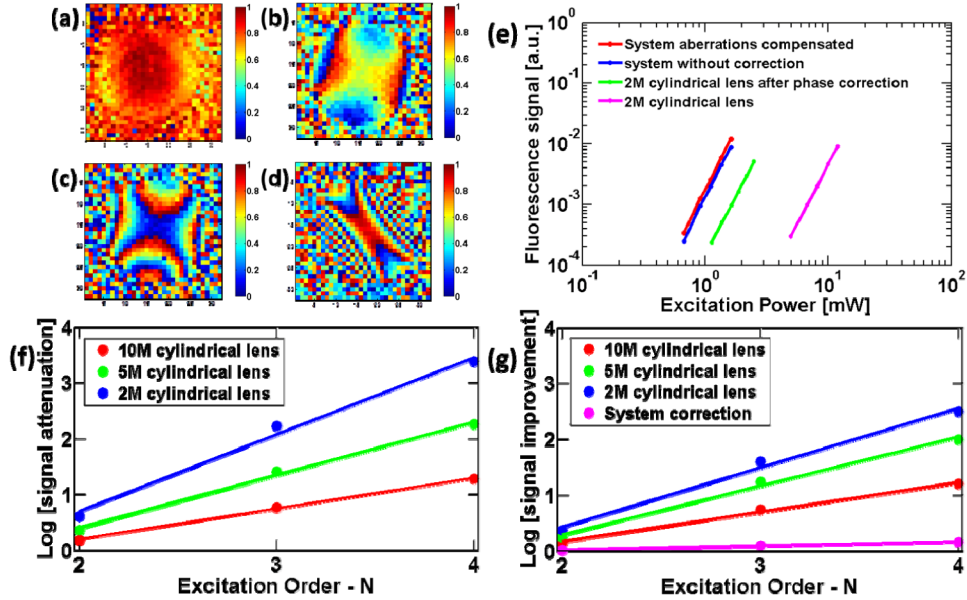
Fig. 6. (a-d) Final phases applied on the SLM for (a) system correction, (b) 10-m focal length cylindrical lens correction, (c) 5-m focal length cylindrical lens correction, and (d) 2-m focal length cylindrical lens correction (Color-bars are in wavelength unit scale). (e) Power curves for 4-photon fluorescence with 2-m focal length cylindrical lens showing the maximal signal (red), the original signal (blue) before system correction, the signal with the cylindrical lens (magenta), and after correction (green). (f-g) Comparison of aberration correction results for 10-m (red line), 5-m (green line) and 2-m (blue line) focal length cylindrical lenses placed above the objective aperture. (f) Signal degradation due to cylindrical lens aberration - excluding lens losses. (g) signal improvement by phase optimization.

The diffraction efficiency of the phase patterns were measured by measuring the power after SLM for each phase pattern. The results of all the measurements are shown in Fig. 6(f-g) and are summarized in Table 1.

From the results it is shown that for the 10-m lens, the signal after aberration correction is almost fully recovered. For example, the 3-photon fluorescence is reduced by a factor of 5.9 due to the 10-m cylindrical lens, and the improvement factor is 5.5. The small difference can be accounted for by the loss of excitation power due to the phase pattern diffraction efficiency, i.e., $5.9 \times 0.976^3 = 5.5$. For the 2- and 5-m cylindrical lenses, the optimized phase didn't fully compensate for signal degradation due to phase mismatch and phase segmentation that can be seen on Fig. 6(c-d).

Table 1. Dye pool results summary

		Cylindrical lens focal length			
Improvement factor by optimization		10 m	5 m	2 m	System
	2-photon	1.4	1.75	2.35	1.03
	3-photon	5.5	17.5	40	1.25
	4-photon	16	100	320	1.45
Signal degradation due to cylindrical lens					
	2-photon	1.53	2.30	4.16	
	3-photon	5.9	26	167	
	4-photon	19	184	2420	
Phase pattern diffraction efficiency					
		0.976	0.959	0.912	

6. Discussion

In Fig. 6(f-g) an approximately exponential relationship is shown between the order of nonlinearity and the improvement/degradation factor. This could be explained if we look at the expression for nonlinear signal in a thick sample [29,30]:

$$\left\langle F^{(N)}(t) \right\rangle = \frac{1}{N} \frac{g_P^{(N)}}{(f\tau)^{N-1}} \phi \eta \sigma_N C n_0 \frac{a_N (NA)^{2N-4} \left\langle P(t) \right\rangle^N}{8\pi^{3-N} \lambda^{2N-3}} \tag{2}$$

where $\left\langle P(t) \right\rangle$ is the excitation average power, n_0 is the refractive index of the sample media, N is the nonlinear order, f is the laser repetition rate, τ is the laser pulse width, ϕ is the system collection efficiency, η is the fluorescence quantum efficiency, C is the concentration of the fluorophore, σ_N is the N-photon absorption cross section, λ is the excitation wavelength in vacuum, NA is the numerical aperture of the objective, a_N is a volume integration factor which is dependent on the nonlinearity order [29], and $g_P^{(N)}$ is the temporal coherence of the excitation source [29,30]. When aberration is added to the beam, however, we may approximate the impact of aberrations on the volume integration and the intensity distribution as having an effective numerical aperture – NA' and volume integration factor - a'_N . The nonlinear signal degradation factor $\psi^{(N)}$ will be therefore described according to:

$$\psi^{(N)} = \frac{\left\langle F'^{(N)}(t) \right\rangle}{\left\langle F^{(N)}(t) \right\rangle} = \frac{g'^{(N)} \tau'^{N-1}}{g^{(N)} \tau^{N-1}} \frac{a_N (NA)^{2N-4}}{a'_N (NA')^{2N-4}} \cong \frac{a_N (NA)^{2N-4}}{a'_N (NA')^{2N-4}} \tag{3}$$

where we assume that the effect of the aberrations on the pulse temporal profile is negligible for the low order aberrations considered here. The plot in Figs. 6(f-g) can then be described as:

$$\log\left[\psi^{(N)}\right] \cong \log\left[\frac{a_N}{a'_N}\right] + (2N-4)\log\left[\frac{NA}{NA'}\right] \tag{4}$$

This approximation leads to similar results which were calculated by Katz at al [21]. for the case of scattering. It is easy to see that the degradation and improvement factors for 2-photon excitation (i.e., $N = 2$) in uniform thick sample (e.g., dye pool, uniformly labeled large blood vessels and large cell bodies, etc.) are small as predicted by Eq. (4). The situation is very different for 3- and 4-photon excitation, where the nonlinear order is higher than 2, since the degradation factor $\psi^{(N)}$, and therefore the potential for improvement with AO increase exponentially with N. This means that the potential of adding AO to such systems in improving signal is higher for higher order nonlinearity.

We further simulated the dependency of the signal losses on the nonlinearity order N. We applied cylindrical lens aberration using the system parameters for the focal lengths that have been used in the experiment (2, 5 and 10 m). Then, by using beam propagation we simulated the optical field at different axial positions around the image plane, and calculated the volume integral. We compared the results from the aberrated and the original beams, resulting in the dependency of the losses on the nonlinearity order – N.

The results, shown in Fig. 7(g) are similar to the experimental results, and agree with the exponential dependency described in Eq. (4).

In order to show that the explanation given above is valid for general low order aberrations and not just for cylindrical-lens induced aberration, we simulated the effect of beam aberrations on the N_{th} order nonlinear process. We used the first 35 Zernike polynomials

[31–33] in order to simulate different aberrations, with the normalization defined by Wyant and Creath [33], where all Zernike terms are normalized to have unity magnitude at the edge of the pupil. We applied aberration with 5λ peak-to-valley (P-V) magnitude which led to similar results that were obtained in the experiment. We used beam propagation in order to calculate the field at different axial positions around the image plane, and performed the volume integral of the N_{th} power intensity distribution. By comparison of the aberrated and the original beams, we calculated the dependency of the loss of fluorescence signal on the nonlinearity order – N. Figure 7 shows the simulation results for the prime aberrations, which are related to Zernike terms according to Noll [31]. In addition, a random combination of the first 35 Zernike terms was used to simulate an arbitrary aberration. This arbitrary aberration, shown in Fig. 6(f), includes more aberration orders than typically observed in *in vivo* brain imaging experiments [17,18]. The results show exponential dependency on N (which is linear on a logarithmic scale), starting from $N = 2$, (except for the 5th order spherical aberration which shows such dependency from $N = 3$).
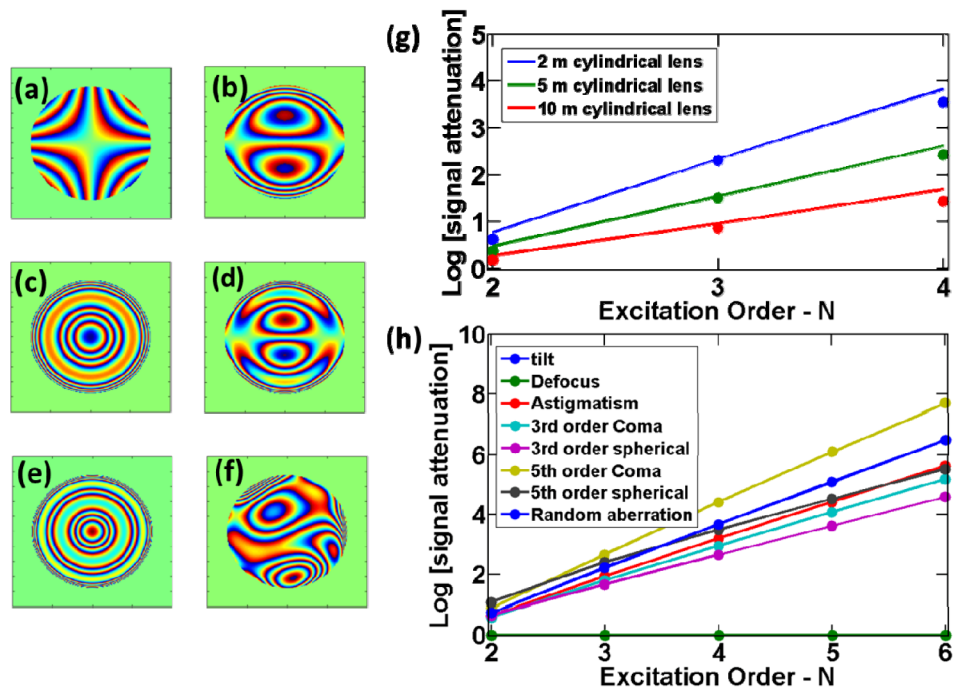

Fig. 7. Simulation results of signal losses due to aberrations for high order excitation. (a-f) Zernike phase maps of: (a) astigmatism, (b) 3rd order coma, (c) 3rd order spherical, (d) 5th order coma, (e) 5th order spherical. (f) Phase map of an arbitrary aberration combined from random coefficients of 25 Zernike orders. (g) Comparison of experimental results (marked with circles) to simulation results (lines) of cylindrical lens aberration for 2-, 5- and 10-m focal lengths. (h) Logarithmic plot of signal degradation due to aberrations as a function of the nonlinear order –N. Applying tilt or defocus terms does not change the result of the volume integral since they are equivalent to lateral or axial movements.

These numerical simulation results and our experimental investigations show that the effect of aberrations on the signal increases exponentially with the order of nonlinearity. As a side note, applying tilt or defocus terms does not change the result of the volume integral since they are equivalent to lateral or axial displacement of the focus. A few issues should be noted or further investigated: according to Fig. 4(b), the optimal phase step may be different for different nonlinear orders, since for $\alpha = 4$, $\pm \lambda/\alpha$ is hitting a "flat" region on the a + b ×

$\cos(\phi/2)^{2N}$ phase curve for high nonlinearity. It seems that for higher order nonlinearity smaller changes ($\alpha \approx 6$) will be optimal.

Another issue is that the algorithm which we used is a general algorithm which can be used either for scattering compensation or for aberration correction. Such algorithm does not distinguish between low- and high-order phase patterns, and is not optimal for low order aberrations. A different approach can be used for aberration correction only using Zernike polynomials [34,35], which may be more efficient. Such algorithm may need some adjustments in order to operate well for high nonlinear order. Nonetheless, the comparison of AO for different order nonlinear processes is independent of the particular algorithm used.

7. Conclusion

We describe here a first demonstration of higher order nonlinear AO system. In particular we demonstrated a comparison of using AO feedback in the case of dye-pool signal for 2-, 3- and 4-photon excitation. We showed experimentally that the effect of aberrations on the signal increases exponentially with the order of nonlinearity in a thick fluorescent sample. Therefore, the impact of AO on higher order nonlinear imaging is much more dramatic. We anticipate that the signal improvement shown here, will serve as a significant enhancement to current 3PM, and perhaps for future 4PM systems, allowing imaging deeper and with better resolution in biological tissues.

Acknowledgments